Influence of Biaxial Stress on Lithium Dendrite Nucleation and Growth in Solid Electrolytes

Siyuan Song, Akshay Pakhare, Lucas Caretta, Brian W. Sheldon, Kyung-Suk Kim, Pradeep R. Guduru*

School of Engineering, Brown University, Providence, RI, 02906

Corresponding Author: *pradeep_guduru@brown.edu

Summary

Short circuits caused by lithium dendrite penetration remain a critical challenge in all solid-state batteries. The influence of mechanical boundary conditions on dendrite nucleation and propagation remains an important area of interest, with significant implications for failure mitigation and battery performance. Here we present an experimental study using direct optical visualization to observe how dendrites nucleate and propagate in a solid electrolyte (LLZTO) under externally applied in-plane equi-biaxial stress. Our setup uses nearly square, plate-shaped electrolyte samples with two lithium electrodes on the same face, which creates mainly in-plane lithium flux parallel to the plate surfaces while equi-biaxial stress is applied during electrochemical cycling. The results demonstrate that in-plane equi-biaxial tension favors a plane-normal dendrite-growth mode, whereas in-plane equi-biaxial compression promotes a planar dendrite-growth mode. Regarding nucleation, over the investigated stress range of −50 to +10 MPa, both compressive and tensile stresses reduce the threshold current density (TCD), somewhat counterintuitively. The observed stress-dependent dendrite mode selection can be interpreted in terms of two competing mechanisms: modification of the crack-tip driving force due to the stress state and the tendency of the dendrite to deflect toward the free surface depending on the sign of applied stress. Together, the stress-controlled dendrite mode selection and the stress vs. TCD map reveal insights into how in-plane stress influences dendrite nucleation and propagation, providing mechanistic guidance for rational design of more stable solid-state electrolytes.

Keywords: Lithium dendrites, Solid electrolytes, Dendrite nucleation and propagation, Stress

Introduction

Initiation and evolution of lithium (Li) dendrites remains a challenge in practical applications of solid electrolytes [1]. Of particular interest here is the coupling between mechanical stress in the electrolyte, dendrite nucleation threshold, and dendrite propagation pathways [2-6]. In this work, we experimentally impose an in-plane equi-biaxial stress field on a solid electrolyte (SE) to investigate its influence on dendrite nucleation and propagation. Based on the observations under different stress states, we attempt to infer the underlying mechanisms of dendrite development and evaluate the potential of the strategy of employing in-plane biaxial stress states for dendrite control and mitigation.

Dendrite nucleation and propagation involves coupled electro–chemo–mechanical processes [7], in which stress and crack formation are key observables of the mechanical response. Dendrite structures are characterized by fracture-like regions occupied by lithium filaments [8, 9]. Electrochemical accumulation of lithium in crack-like defects is constrained by the elasticity of the SE, leading to pressure buildup in the range of 100–1000 MPa as inferred from micro cantilever bending [4, 10]. The high stress fields around the crack tip were verified by DIC [11] and photoelastic measurements [12, 13]. Based on this picture, dendrite growth has often been interpreted as an internal pressure driven crack-opening process [6, 14]. Various strategies have been proposed to regulate dendrite behavior, including applying uniaxial stress to influence propagation pathways [15], increasing lithium temperature to reduce internal pressure buildup [16], induce biaxial compressive stress [17] and imposing thermal gradients [18] to introduce additional compressive stress fields.

Although the conceptual model of an internal pressure-driven crack opening process appears qualitatively consistent, several unresolved issues limit its applicability to more complex stress states. A primary challenge is the unknown pressure distribution within the dendrite. Resolving it requires an understanding of the local multi-physics coupling between ionic flow and localized pressure at both the Li-SE interface and the Li-SE-void triple junction, alongside lithium metal transport within the confined crack space. For the ionic flow, it is generally assumed that the internal dendrite pressure modifies the flow according to stress-coupled Butler–Volmer kinetics [14], however, to the best of the authors' knowledge, it lacks robust experimental validation. As for the lithium metal transport, both plastic flow [19] and rigid-body models have been proposed [14]. Nevertheless, these assumptions remain to be verified through quantitatively calibrated

controlled experiments, especially considering the potential spatial lag between the dendrite tip and the lithium filament front. From the crack-opening perspective, both lithium plating and grain-boundary degradation [20, 21] have been proposed as contributing mechanisms [22], yet their relative contributions in different growth states lack a systematic understanding for reliable prediction. In addition, although a dependence of the critical stress intensity factor on the global current density has been observed [13], the underlying mechanism remains unresolved. From a morphological perspective, experiments reveal rich, multi-branched architectures [3, 6, 23], whereas idealized models often describe dendrites as a simple crack-like defect [7, 19, 24]. The emergence of complex dendrite morphologies and how the dendrites transition between different growth modes require further insights, multiscale modeling and statistical descriptions.

Considering these unresolved issues, the influence of more general stress states requires further investigation. From an experimental perspective, there is a paucity of well-controlled studies that systematically probe the effect of in-plane equi-biaxial stress, which provides a simple and well-defined mechanical states on the SE. Existing experimental efforts have largely focused either on stacking pressure [2, 24-26] to modify interfacial contact [27], or on uniaxial stress [15] to provide preliminary insights into rerouting of out-of-plane dendrite growth. A recent study introduced a biaxial compressive stress of 330 MPa to delay the onset of short circuiting [17]. Ion implantation and ion-exchange approaches have been employed to introduce compressive residual stresses ranging from several hundred megapascals to several gigapascals in near-surface layers of solid electrolytes [28-33]. For example, Morris et al. [28] reported an increase in the average critical current density (CCD) from 0.30 to 0.95 mA/cm² following Ag^{+}/Li^{+} ion exchange, while Thomas et al. [29] observed an increase in the current density at which soft breakdown occurred from 0.5 to 1.0 mA/cm² following F-ion implantation. However, these values depend strongly on the experimental conditions and testing protocols, with other studies reporting CCD values as low as 0.15 mA/cm² for untreated LLZTO [34]. Shot peening has also been used to modify the surface stress state and roughness; however, it has not fully prevented nucleation or short-circuiting [35, 36]. Most existing studies have not clearly isolated biaxial stress as the sole variable, leaving unresolved whether it directly affects nucleation, as opposed to merely delaying short-circuiting, and how stress regulates in situ dendrite pattern evolution. Uniaxial stress tends to bias dendrite propagation along the loading direction and therefore does not fully suppress out-of-plane growth from a purely mechanical perspective. In contrast, in-plane equi-biaxial stress can more uniformly

constrain crack opening in all in-plane directions, making it conceptually more promising for regulating dendrite behavior [17]. In addition, in-plane equi-biaxial stress states commonly arise in thin structures, such as the thin-film SE fabricated by laser deposition or the thin-sheet SE within a layered configuration. Under these conditions, equi-biaxial stresses can be induced by thermal expansion mismatch or by global substrate bending. Understanding the effect of in-plane equi-biaxial stress is therefore valuable for evaluating the stability and performance of SEs.

In this study, we conduct experiments under well-controlled in-plane equi-biaxial stress to investigate its influence on dendrite development in $Li_{6.6}La_3Zr_{1.6}Ta_{0.4}O_{12}$ (LLZTO) electrolytes, which serves as a model system. In contrast to the practical scenario where thin disk-shaped electrolytes have electrodes on opposite faces and dendrites propagate through the thickness, our model configuration involves deposition of both electrodes on the same face of electrolyte specimens. Consequently, Li flux is predominantly in an in-plane direction and dendrites grow in in-plane directions. On the other hand, such a configuration allows capture of dendrite growth and growth mode selection by in situ optical imaging, while dendrite nucleation threshold current densities are obtained from electrochemical measurements. A corresponding map is generated across a range of stress states, including both compression and tension. These results fill an important gap in the study of stress effects on the SE response. In particular, a distinct dendrite growth mode, namely, a planar dendrite is seen to be promoted under in-plane equi-biaxial compressive stress states, which has received much less attention compared to normal crack-like dendrites. The findings could provide guidance for developing stress-based strategies for dendrite regulation.

Results

Detailed procedures for electrolyte preparation, electrode deposition, residual-stress generation, electrochemical testing, and imaging are provided in the Methods section. In the current study, we focus primarily on dendrite growth morphology and the corresponding threshold current density (TCD), defined as the current density at which dendrite nucleation first becomes detectable, at different in-plane equi-biaxial stress values. Figure 1 presents representative optical images of the dendrite morphologies developed in LLZTO specimens under different stress states. In stress-free samples (Figure 1(a)), dendrites exhibit a mixture of narrow branch-like and wide leaf-like morphologies. The narrow branch-like dendrites correspond to plane-normal crack-like features, with their crack planes approximately perpendicular to the traction-free top surface, whereas the wide leaf-like dendrites correspond to fracture planes approximately parallel to the top surface. Although these two morphologies are globally intermixed, they remain locally distinguishable, resembling the separation between branches and leaves in a tree. A representative boundary between the two morphologies is marked by the white arrow in the sub-image. Under equi-biaxial tension, dendrite growth is dominated by narrow branch-like features (Figure 1(b)), while the wide leaf-like mode is largely suppressed. In contrast, equi-biaxial compression promotes the wide leaf-like morphology (Figure 1(c)). The narrow branch-like dendrites are still present in some specimens, but they are less developed. These observations suggest that the narrow branch-like and wide leaf-like mode, highlighted in Figure 1(b) and (c) respectively, can be regarded as two canonical growth modes underlying the mixed morphologies observed in all experiments. The stress-induced preferential selection of these two growth modes is a main insight from the present study. Building on this basic summary, additional details are presented in the following subsections.

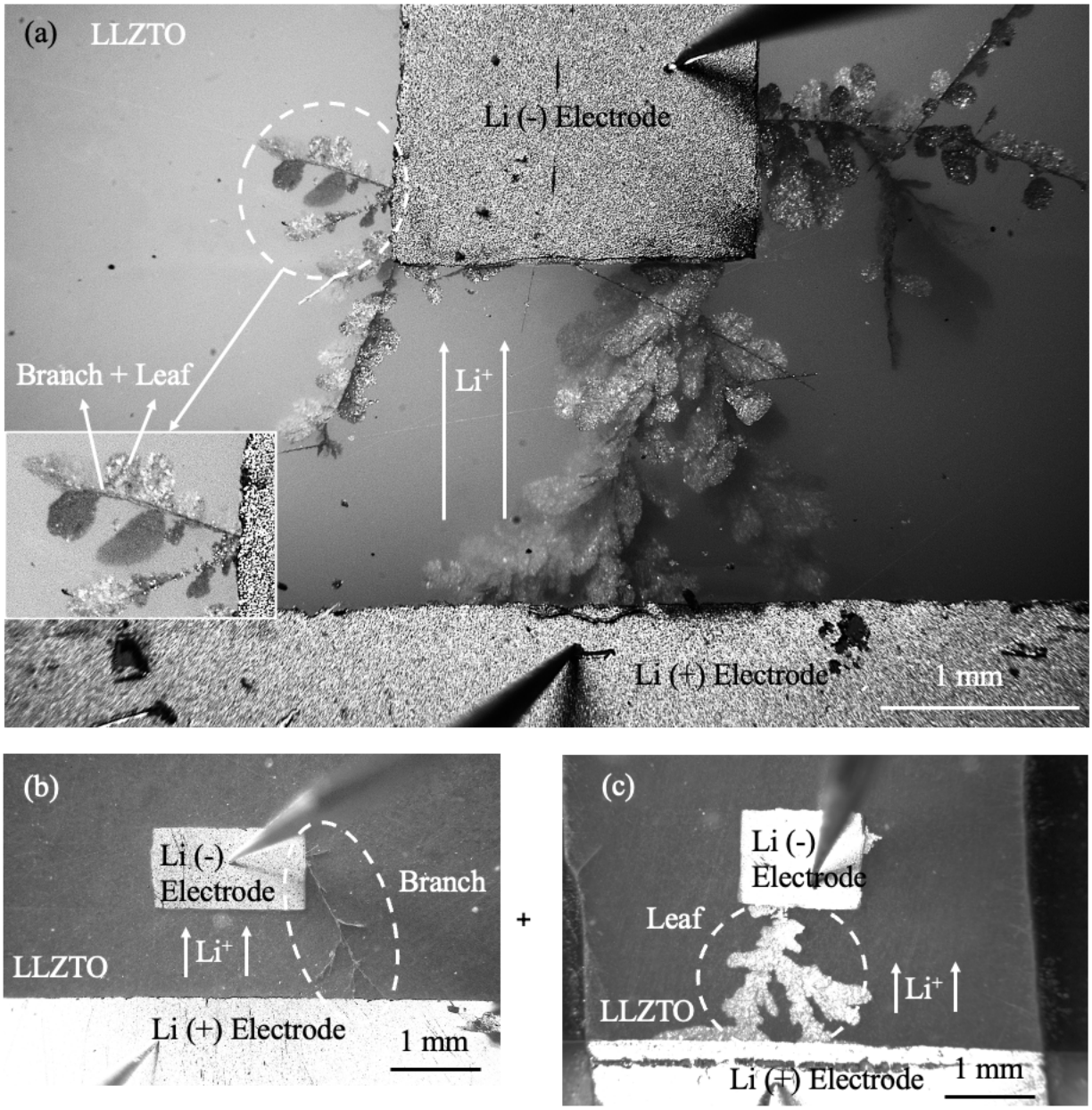


Figure 1. Representative dendrite morphologies in LLZTO SE after electrochemical testing. The imaging system looks directly down at the specimen top surface while it is illuminated at a 45° angle. Lithium-ion flux was directed from the Li (+) electrode at the bottom to the Li (−) electrode as indicated by the white arrows. (a) Generic dendrite patterns in a stress-free LLZTO sample. (b) Branch-type plane-normal dendrites observed under in-plane equi-biaxial tensile stress. (c) Leaf-type planar dendrites observed under in-plane equi-biaxial compressive stress. Note that the stress-free specimen contains dendrites of both types.

Stress affects dendrite morphology

Figure 2 compares in-situ evolution of lithium dendrites in LLZTO in three representative specimens during electrochemical testing under the current profile described in Methods. Each column corresponds to a different stress state in the SE: compressive, stress-free and tensile. The figures in each column represent three stages of dendrite evolution: pristine, during development, and fully developed. Each image presents a contrast-enhanced differential image, with the corresponding original optical image shown in the lower-left corner. All images share the same scale bar, which is displayed in Figure 2(a1).

Within the differential images, red indicates an increase in brightness, whereas blue indicates a decrease in brightness. These intensity variations primarily arise from changes in light reflection and transmission caused by lithium dendrites within the LLZTO electrolyte. Under equi-biaxial compression (Figure 2(a1–a3)), wide leaf-like dendrites become the dominant morphology. The enhanced red contrast arises from stronger light reflection of lithium relative to the dark epoxy background in regions where lithium is absent. These dendrites exhibit extensive lateral spreading. Owing to their preferential in-plane growth (in a plane predominantly parallel to the stress-free top surface), we refer to this morphology as planar dendrites. In contrast, under equi-biaxial tensile stress (Figure 2(c1–c3)) narrow branch-like dendrites dominate. These dendrites appear as slender filaments from the top while extending into the specimen on planes predominantly perpendicular to the top surface. As such, they correspond to the traditional plane- normal crack-like picture of dendrites, and we refer to them as plane-normal dendrites. For the nominally stress-free samples (Figure 2(b1–b3)), both morphologies are observed simultaneously, including wide planar dendrites and narrow plane-normal dendrites.

The dominant dendrites propagate toward the Li (+) electrode and eventually bridge the electrolyte causing electrical shorts. The location where a dendrite first becomes optically visible outside the Li (−) electrode area is defined as the optical nucleation point, and the corresponding current density is defined as the optical threshold current density (O-TCD). We allow for the possibility that a dendrite could nucleate earlier under the Li (−) electrode area where it would not be visible. With that caveat, the O-TCD values serve as a quantitative criterion for evaluating the critical condition for dendrite initiation. For the three representative samples shown in Figure 2, the O-TCD was 0.40 mA cm^{-2} under in-plane equi-biaxial compression, 1.26 mA cm^{-2} under the

nominally stress-free condition, and 0.50 mA cm^{-2} under in-plane equi-biaxial tension. A more complete map based on all experiments will be presented in a later section (i.e., Figure 5). Thus, the state of stress influences not only the dendrite mode selection, but also the TCD at which dendrite nucleates. Surprisingly, both tension and compression appear to decrease O-TCD compared to that of a stress-free specimen.

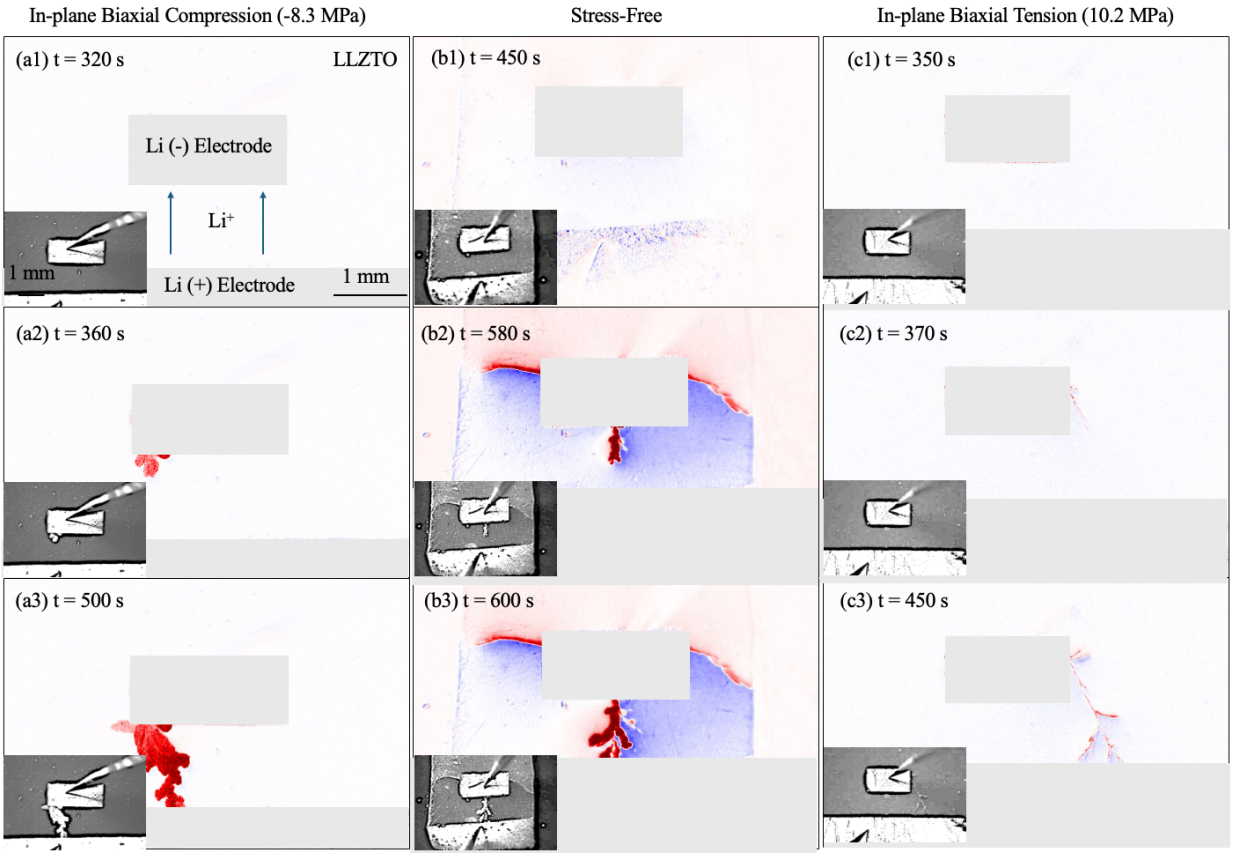


Figure 2. Differential optical images showing the evolution of lithium dendrite morphologies in three representative LLZTO samples. From left to right, the three columns correspond to compressive, stress-free and tensile stress states respectively. The three figures down each column show progression of dendrites in each specimen from the pristine state to full shorting. Each differential optical image also shows the corresponding original optical image in the lower-left corner. The scale bar and electrode/electrolyte labels in panel (a1) apply to all images. Time stamps are indicated in the upper-left corner of each panel.

To reveal the sub-surface morphology of the planar and plane-normal dendrites, FIB–SEM characterization was performed, as shown in Figure 3. Two representative observation regions

were selected: one containing a planar dendrite and the other containing a plane-normal dendrite. Before FIB–SEM characterization, the lithium electrode was gently removed with a tissue paper to expose the underlying dendrite nucleation region. The FIB-SEM images were acquired at a 45° viewing angle, resulting in a relative scale-bar ratio of approximately 1.4 between the vertical and horizontal directions. Figures 3(a1–a5) reveal the subsurface orientation of a planar dendrite. The observation region is marked by the red dashed box in Figure 3(a1). This region appears bright in optical imaging due to high reflectivity of the subsurface lithium. At the free surface (Figure 3(a2)), no distinguishable features can be identified beyond the intrinsic surface roughness of LLZTO. This is because, unlike visible light imaging, the electron beam cannot penetrate the electrolyte to reveal the buried lithium dendrites. The absence of obvious surface deformation or cracking indicates that planar dendrites remain largely buried beneath the free surface, except where they intersect with the free surface. To reveal the subsurface morphology, three FIB cross-sections were prepared near the edges of the region of interest, as indicated in Figure 3(a2). The corresponding cross-sectional images are shown in Figures 3(a3–a5), which show cracks that extend from the free surface into the bulk at a shallow angle and/or meander to become approximately parallel to the free surface (Figure 3(a3)). The small variations in dendrite inclination among the three cross-sections are likely attributable to the combined effects of free-surface-induced deflection and local microstructural heterogeneity.

Figures 3(b1–b5) show the internal orientation of a plane-normal dendrite. The corresponding optical observation region is marked by the red dashed box in Figure 3(b1). Unlike the planar dendrites, which do not exhibit any surface features in the SEM images, the plane-normal dendrite is accompanied by a pronounced zigzag surface crack pattern. FIB cross sections were imaged at three locations along the dendrite as shown in Figures 3(b2–b5). In contrast to the planar dendrites, the dendrite plane extends into the bulk at approximately normal to the free surface. The crack plane meandering seen in the images suggests that the plane-normal dendrites, even if they nucleate at a non-normal angle near the free surface, evolve to approach a nearly perpendicular plane.

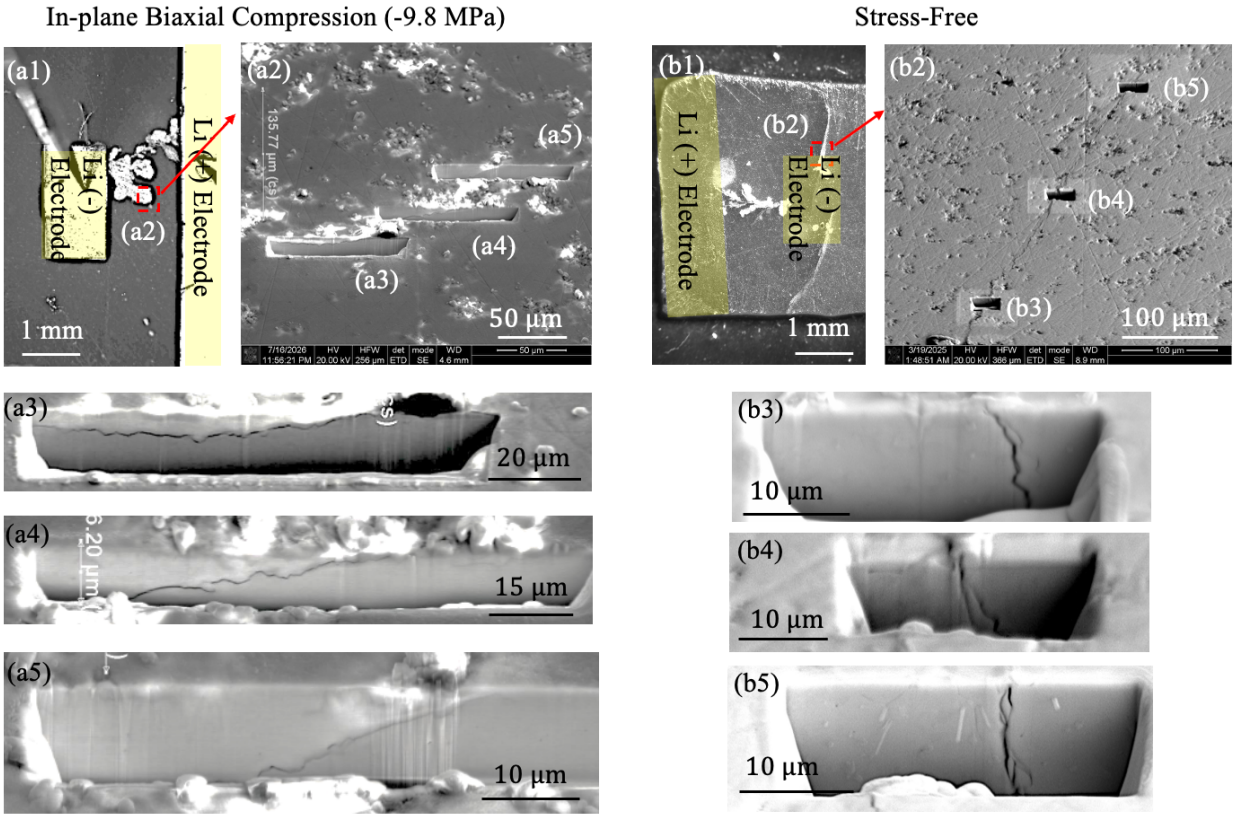


Figure 3. FIB–SEM characterization of the planar and plane-normal dendrites in LLZTO. (a1–a5) Planar dendrite: (a1) Optical image of the specimen showing a planar dendrite. (a2) SEM image showing three FIB cross-section locations. The area imaged corresponds to the area indicated in (a1). (a3–a5) Magnified views of the three corresponding FIB cross-sections showing the dendrite plane orientation to be at shallow angles to the top surface except where the dendrites meet the top surface. (b1–b5) Plane-normal dendrite: (b1) Optical image of the specimen containing a plane-normal dendrite. (b2) SEM image showing three FIB cross-section locations. (b3–b5) Magnified views of the corresponding cross-sections. The sub-surface dendrite plane is nominally normal to the free surface. These observations are highly repeatable across all samples and reveal the generality of stress-dependent dendrite mode selection between the planar and the plane-normal dendrite morphologies. The vertical and horizontal scale bars have a ratio of 1.4 due to the inclined viewing angle.

Electrochemical Response

The electrochemical response of the three representative samples shown in Figure 2 are presented in Figure 4. Figures 4(a), (b), (c) correspond to compressive, stress-free and tensile stress cases. A

stepwise galvanostatic current was applied as described in Methods. Initially, the cell voltage $E(t)$ evolves smoothly during each galvanostatic interval. In Figure 4(a), at $t = t_1 = 312$ s, a sharp voltage drop is observed, marking the onset of an electrochemically driven instability. A second abrupt transition at $t_2 = 460$ s collapses the voltage to near zero signaling a short-circuit. For the optical signal discussed in Figure 2, the first optically observable dendrite appears at approximately t = 322 s. This sequence of an initial abrupt voltage drop, followed by the appearance of a dendrite in optical imaging a few seconds later occurs in all specimens. Hence, we identify the first abrupt voltage drop with nucleation of a dendrite under the Li (−) electrode area. The short time delay between the voltage drops and the first appearance of a dendrite in optical imaging can be attributed to the dendrite propagation time to the edge of the Li (−) electrode area where it becomes visible. Consequently, the electrically measured threshold current density (E-TCD) corresponding to the initial sharp drop is always less than or equal to the optically measured threshold current density (O-TCD). Similar transitions are observed in Figures 4(b) and (c) for the stress-free and the tensile stress specimens. Of particular interest here is the influence of stress on the critical conditions for dendrite nucleation. The measured values of E-TCD and O-TCD were extracted for all 18 samples that spanned six equi-biaxial stress values and are shown in Figure 5 as a function of the equi-biaxial stress magnitude. Also shown are the standard deviation values that capture the scatter.

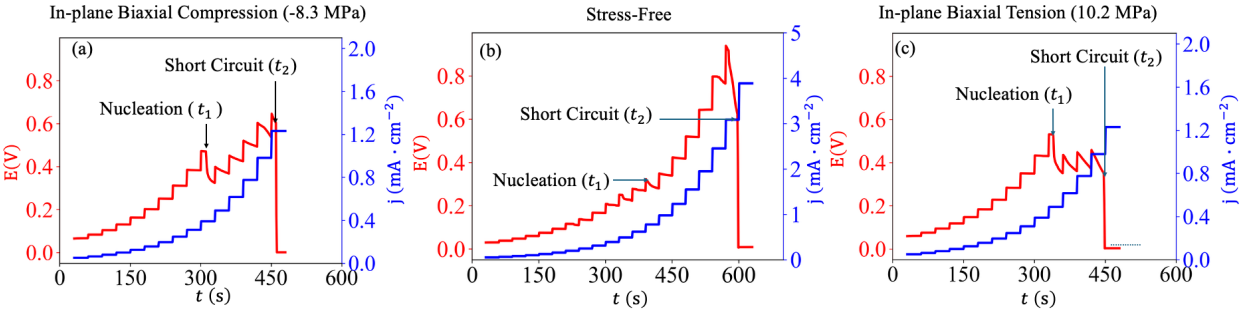


Figure 4. Electrochemical response during stepwise galvanostatic loading in three representative experiments: (a) in-plane equi-biaxial compression, (b) stress-free, and (c) in-plane equi-biaxial tension. The imposed current density (right axis, blue line) and measured voltage (left axis, red line) are plotted on the same time base. Current is applied in progressively increasing steps with a fixed hold time of 30 s at each level. The voltage response in each experiment exhibits three characteristic stages: smooth evolution during each constant current hold; a sudden partial voltage drop associated with dendrite nucleation (at t_1); and a final voltage drop to approximately zero upon full short circuit (at t_2). These characteristic voltage features provide consistent

electrochemical signatures for identifying dendrite nucleation and the eventual full short circuit across all stress states.

Both E-TCD and O-TCD values follow each other closely and exhibit the same stress dependence. They have a maximum value in the stress-free condition and decrease under both compression and tension. However, the rate of reduction is more precipitous under tensile stress. Following an initial rapid drop, the TCD values appear to reach a nominally constant value under compressive stress states. At the same time, it is worth recalling from the previous section that the dendrite mode is different depending on the sign of the stress. From Figure 5, it can be concluded that, for the surface electrode configuration and the stress range investigated in this study, in-plane equi-biaxial stress promotes earlier dendrite initiation irrespective of the stress sign. This is a surprising result in view of the prevailing picture of dendrite growth. Since dendrites are generally depicted to be crack-like features that propagate from Li (−) electrode to Li (+) electrode, application of tensile stress states would be expected to promote dendrite growth, whereas compressive stress states would be expected to impede it. The new finding here is that the sign of the applied stress changes dendrite mode selection, and the threshold current density for dendrite nucleation in both cases is lowered compared to the stress-free state.

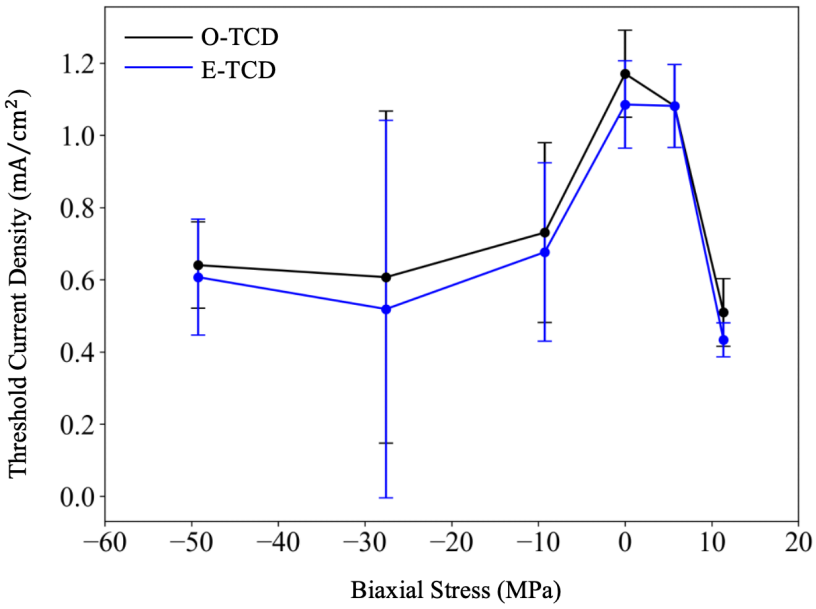


Figure 5. Threshold current densities (TCD) as a function of in-plane equi-biaxial stress, averaged over multiple samples. Since the principal stresses are slightly different from each other in most specimens, their average value is plotted on the abscissa. Black: electric TCD (E-TCD). Blue: optical TCD (O-TCD). For the surface electrode configuration and the stress range investigated, in-plane equi-biaxial stress appears to promote earlier dendrite nucleation irrespective of the stress sign.

Discussion

The observed dendrite morphologies, together with the corresponding voltage–current responses, lead to the following key observations for the planar electrode-electrolyte configuration investigated in this study:

(1) In-plane equi-biaxial tensile stress promotes formation of plane-normal dendrites.
(2) In-plane equi-biaxial compressive stress favors formation of planar dendrites.
(3) Under nominally stress-free conditions, both plane-normal and planar dendrites can develop.
(4) Within the stress range investigated (-50 MPa to 10 MPa) for the electrode-electrolyte configuration employed, and the electrochemical testing procedures, both in-plane equi-biaxial compression and tension reduce the TCD for dendrite nucleation.

Numerous studies from recent literature have reported several aspects of dendrite morphologies in stress-free SEs [9, 22, 23]. However, these morphologies have largely been treated as distinct experimental observations, with limited mechanical interpretation of their underlying three-dimensional evolution. The influence of externally applied uniaxial tensile stress on dendrite deflection has also been experimentally demonstrated and interpreted using mixed-mode fracture mechanics [15]. Nevertheless, these analyses are primarily restricted to two-dimensional scenarios involving edge cracks or straight cracks embedded in an infinite body. However, the conditions influencing morphology selection and transition observed in the present study has received little attention. Here we attempt a qualitative physical interpretation of our observations based on a combination of a fracture criterion and crack path stability effect in the presence of a free surface.

Partly building on the framework developed by Mukherjee et al. [14], the SE is treated as a linear elastic continuum, and a dendrite is viewed as a lithium-filled crack. The volumetric

growth of deposited lithium in a dendrite is constrained by the surrounding crack surfaces, generating an internal pressure that deforms the SE and produces stress concentration at the dendrite tip. Crack propagation occurs when the stress intensity factor exceeds the (electrochemically active) effective fracture toughness [11, 13] while lithium-ion flux from the SE to the lithium phase remains thermodynamically permissible. The interfacial lithium-ion flux is described by the stress-coupled Butler–Volmer equation [37, 38], in which the equilibrium overpotential increases approximately linearly with the normal lithium pressure in the limit of an infinitesimal interfacial flux [39]. The local overpotential is determined by the electric potential distribution governed by Maxwell's equations and is directly related to the applied far-field current density through the electrochemical boundary conditions. Consequently, the critical lithium pressure required for crack propagation determines the corresponding TCD. Mukherjee et al. [14] considered a two-dimensional edge crack as a representative dendrite morphology, where the crack was assumed to propagate straight ahead in a nominally stress-free SE. While this framework provides valuable insights into dendrite initiation and propagation, it does not capture the complex dendrite morphologies observed in the present experiment. The three-dimensional dendrite morphologies arise from the combined effects of the initial dendrite orientation, applied stress field, boundary conditions, and other contributing factors. In the present study, we simplify the problem by considering two canonical crack-like defects that trigger and lead to dendrite growth in the SE near the Li (−) electrode: plane-normal and planar as illustrated in Figure 6(a1) and Figure 6(b1), respectively. It is also assumed that stressed grain boundaries provide sufficient electron conductivity for subsurface dendrite growth near the Li (−) electrode [40]. In reality, by virtue of the complex microstructure of the SE, one can presume the presence of a large population of micro-defects of all orientations and a size distribution near the Li (−) electrode. However, we restrict attention to planar defects whose planes are parallel to the free surface, and plane-normal defects whose plane is normal to the free surface.

Growth of these defects under three relevant stress states - equi-biaxial compression, stress-free, and equi-biaxial tension - is considered while accounting for the presence of the free surface. Figures 6(a2–a4) illustrate the influence of in-plane equi-biaxial stress on the crack-tip stress intensity factor of a plane-normal dendrite. Because the crack plane is normal to the x_1 direction as shown in Figure 6(a1), the σ_{11} component of the applied equi-biaxial stress acts normal to the crack plane and directly contributes to the crack-tip stress intensity factor, whereas the σ_{22}

component acts parallel to the crack plane and has no contribution. Consequently, the resultant crack-tip stress intensity factor is determined by the combined effects of the internal lithium pressure, the applied σ_{11} stress, and the free-surface effect. Under equi-biaxial compression (Figure 6(a2)), the applied σ_{11} is compressive, reducing the crack-tip stress intensity factor. Therefore, a higher internal lithium pressure is required for the total stress intensity factor to reach the effective fracture toughness. Since the local overpotential increases with the applied current density, a higher threshold current density (TCD) is required to generate the increased lithium pressure necessary for dendrite propagation. In contrast, equi-biaxial tension (Figure 6(a4)) produces a positive σ_{11}, which increases the crack-tip stress intensity and enables dendrite propagation at a lower internal lithium pressure, thereby reducing the TCD. So, for an initial defect that resembles a plane-normal crack, one would anticipate an equi-biaxial tensile stress to decrease TCD and an equi-biaxial compressive stress to increase it. Moreover, the initial growth direction of the defect need not be oriented towards the Li (+) electrode; it is controlled by the orientation of the initial defect that first reaches the fracture criterion.

For a planar defect (Figure 6(b1)), the primary role of the in-plane equi-biaxial stress is different. Rather than directly modifying the crack-tip stress intensity factor, it governs the stability of crack path [41, 42], i.e., the tendency of the dendrite to propagate in its plane vs. deflect toward the free surface. Analysis of crack stability from fracture mechanics literature [41, 42] shows that equi-biaxial compressive stress (Figure 6(b2)) stabilizes crack propagation in its plane of propagation; alternatively, crack deflection away from the current propagation plane is suppressed, making continued planar propagation kinetically favorable. Further, in addition to contributing to dendrite path stability, the compressive stress could also contribute to "delamination buckling" of the planar dendrite once it reaches a critical in-plane dimension [43], which contributes to the crack-opening stress intensity factor and thus decreases the critical lithium pressure for satisfying the fracture criterion, and thus the TCD. Thus, compressive stress not only enables initially planar defects near the Li (−) electrode to propagate in their planes but can also contribute to the stress intensity factor and lowering of TCD. Moreover, increasing the compressive stress lowers the expected TCD. Under in-plane equi-biaxial tension (Figure 6(b4)), planar propagation becomes unstable. Because tensile stress favors crack planes oriented perpendicular to the loading direction, a planar dendrite front is driven to deflect toward the free surface. Consequently, a planar dendrite

may evolve into a bowl-shaped crack that meets and terminates at the free surface [23]. Under stress-free conditions (Figure 6(b3)), a planar defect is influenced by the configurational force associated with the nearby free surface. This image force drives the planar dendrite to deflect toward the free surface [44], which can also be viewed as loss of crack path stability. This effect becomes stronger as the dendrite is closer to the free surface and weaker as the distance increases. Thus, planar growth becomes viable if the initial defect is sufficiently far away from the free surface.

To summarize, depending on the initial defect population, both dendrite modes are viable. Compressive stress makes it harder for plane-normal defects to grow but stabilize planar defects and enables their growth towards the Li (+) electrode. Through a postulated delamination-buckling mechanism [43], compressive stress can decrease the TCD. Tensile stress promotes growth of plane-normal defects and lowers the TCD for their nucleation and growth. In addition, tensile stress destabilizes planar defects, deflects them towards the free surface and terminates them there as bowl shaped cracks. Under stress-free conditions, a plane-normal defect can propagate due to the internal Li pressure, and a planar defect can propagate towards the Li (+) electrode if it is sufficiently away from the free surface. Thus, this simplified picture provides a framework for understanding how the sign of stress promotes a different dendrite mode and also offers a qualitative explanation for why the TCD decreases with stress magnitude in both directions. Although beyond the scope of this paper, this framework can be extended computationally to incorporate more complex boundary conditions and initial defect morphologies.

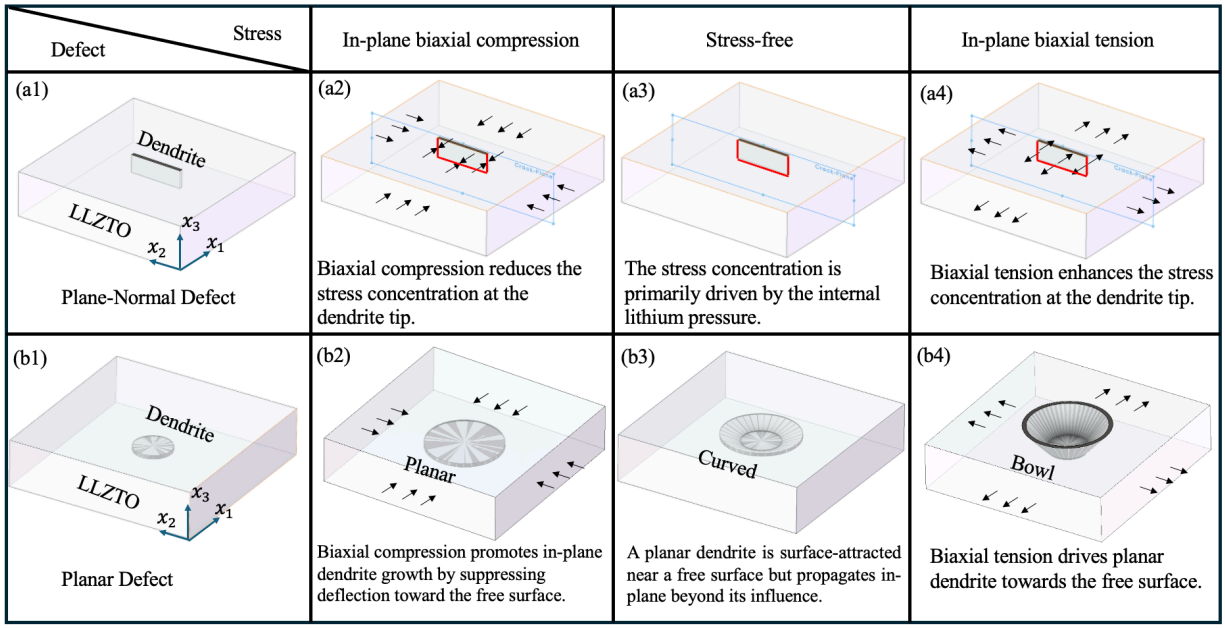


Figure 6. Schematic illustration of the effect of in-plane equi-biaxial stress on crack driving force and stability of crack propagation direction in the SE. Here, a dendrite is treated as a crack nucleating from an initial plane-normal or planar defect. (a1) Plane-normal dendrite; (b1) planar dendrite. (a2) -(a4) illustrate the influence of equi-biaxial stress on the driving force on a plane-normal defect. (b2)-(b4) illustrate the influence of equi-biaxial stress on stability of planar crack growth.

It should be emphasized that dendrite growth is ultimately governed by lithium deposition, which is controlled by the local electric field distribution and the resulting internal lithium pressure. Regions with a higher electric field promote faster lithium deposition, thereby providing a greater driving force for dendrite propagation. In the present cell configuration, both the Li (−) electrode and Li (+) electrode are located on the same side of the LLZTO electrolyte. Consequently, when a planar dendrite propagates toward the Li (+) electrode, the remaining distance to the Li (+) electrode is progressively reduced, leading to local electric-field enhancement at the dendrite tip. The increased lithium deposition rate enables continued propagation under equi-biaxial compression. As such, this mechanism is expected to depend on the electrode configuration. If the Li (−) electrode and Li (+) electrode are located on opposite sides of a compressively stressed SE, the planar mode can propagate only along planes parallel to the faces, and the electric-field enhancement at the dendrite tip would be weaker. Under such conditions, planar dendrites may no

longer propagate efficiently toward the Li (+) electrode and may instead self-terminate at the specimen periphery before forming a short circuit. In this case, dendrite propagation towards the Li (+) electrode would likely be in the form of plane-normal dendrites. Consequently, in-plane equi-biaxial compressive stress would be expected to result in a higher TCD in a practical solid electrode configuration with electrodes on opposite faces, which was seen in a recent study of Cui et al. [17]. Ion implantation has also been employed to induce compressive surface stresses and thereby suppress dendrite initiation [28, 29].

In conclusion, this work investigates the influence of in-plane equi-biaxial stress on dendrite nucleation and propagation in solid electrolytes. In-plane biaxial stress is introduced via thermal residual stress. Electrochemical measurements provide the voltage response under stepwise current loading, from which dendrite nucleation can be identified. In situ optical imaging, based on intensity contrast, enables direct observation of dendrite evolution. First appearance of a dendrite in optical imaging correlates well with the corresponding voltage drop signature. Two distinct dendrite morphologies, namely plane-normal and planar, are identified from optical imaging, which are further validated through SEM characterization. Experimentation under different stress states reveals that in-plane biaxial tension favors the plane-normal mode, whereas biaxial compression favors the planar mode. Both modes can appear together in a stress-free state. The measured threshold current density for dendrite nucleation decreases under both tensile and compressive stress states relative to the stress-free state.

Qualitatively, the stress-controlled mode selection between plane-normal and planar dendrites can be explained by assuming the presence of a population of initially plane-normal and planar micro-defects under the Li (−) electrode area and considering how the biaxial stress state in the solid electrolytes contributes to their propagation criteria. Tensile stress promotes plane-normal dendrite growth and decreases the corresponding TCD, whereas compressive stress has the opposite effect. While the state of stress does not directly influence the driving force for planar dendrite growth, it strongly influences the stability of its propagation direction. Compressive stress allows planar dendrites to grow along their plane, while tensile stress destabilizes and deflects them towards the free surface. Moreover, compressive stress can contribute to crack tip driving force through a delamination-buckling mechanism, thus lowering the TCD. Taken together, this qualitative picture explains stress-controlled dendrite mode selection as well as the reduction in

TCD for both compressive and tensile stress states. By extending this argument to a sandwich cell configuration with electrodes on either side of the SE, it is reasonable to hypothesize that through-thickness dendrites in such a cell would be plane-normal in character and their TCD would increase with compressive stress. In contrast, planar dendrites would be forced to propagate in planes that are approximately parallel to the faces and may self-terminate at the cell edges. Overall, the findings of this study can help arrive at strategies to mitigate dendrite growth in solid electrolytes.

Methods

Specimen Preparation

Commercial LLZTO specimens ($Li_{6.6}La_3Zr_{1.6}Ta_{0.4}O_{12}$, Toshima Inc.; 50 × 50 × 1 mm) were sectioned into approximately 5.8 × 5.8 mm pieces through thermal scoring followed by mechanical cutting with a diamond blade. Samples were then polished manually using silicon carbide sandpapers with progressively finer grit size (240–5000) until the thickness reached ~0.2 mm. The polished LLZTO pellets were transferred into an argon-filled glovebox for subsequent processing. A same-side lithium electrode configuration was used to enable simultaneous in-situ optical imaging and controlled biaxial loading, as shown in Figure 7(a, c). For convenience, we denote Li (−) as the negative electrode, corresponding to the lithium-plating side, and Li (+) as the positive electrode, corresponding to the lithium-stripping side. Approximately 1.5 μm thick lithium film electrodes were deposited by thermal evaporation. The final nominal dimensions of the specimen, as shown by the schematics in Figure 7(c), were: $a = 1.06 \pm 0.25$ mm, $b = 1.30 \pm 0.19$ mm, $c = 0.97 \pm 0.14$ mm, $d = 2.19 \pm 0.75$ mm, $e = 1.90 \pm 0.44$ mm, $f = 1.85 \pm 0.26$ mm, $g = 1.94 \pm 0.47$ mm and $h_{\mathrm{LLZTO}} = 0.22 \pm 0.05$ mm. Sample to sample dimensional variations were accounted for in the current density calculations and the finite element simulations. As discussed in the supplemental material, these dimensions were chosen to ensure that the entire Li (−) electrode area is away from the edges and is under a uniform state of stress.

Thermal Residual Stress

In order to induce a state of biaxial stress in an LLZTO specimen, it is bonded to a 6061 aluminum alloy disc (diameter 50.8 mm, thickness 1.26 mm) or a silicon wafer (edge length 50.8 mm, thickness 0.72 mm) substrate with a thin epoxy layer and cured at a temperature T_2 as illustrated in Figure 7(a). Thin films of epoxy (LOCTITE STYCAST 2651 and LOCTITE Catalyst 9, 100:7 by weight) were spin-coated (2000 RPM) on the substrates, resulting in film thicknesses of 0.05 ± 0.01 mm on Al and 0.17 ± 0.01 mm on Si. Post curing, a residual stress (i.e., in-plane biaxial stress) is generated in the LLZTO specimens when they are cooled from the curing temperature T_2 to the testing temperature T_1 due to the mismatch in the coefficients of thermal expansion (CTE) between LLZTO and the substrate. The Al alloy's CTE (23.6×10^{-6} K^{-1}, [45]) is greater than that of LLZTO, which results in a biaxial compressive stress state. Si's CTE (2.5×10^{-6} K^{-1}, [46]) is smaller, resulting in a biaxial tensile stress state. The stress magnitude can be varied by changing

the curing temperature. Three independent samples were prepared for each curing condition (i.e., the substrate and the curing temperature). For Al substrates, the curing conditions were 30 °C (24 h), 40 °C (16 h), 60 °C (4 h), and 80 °C (2 h). For the Si substrates, the curing conditions were 45 °C (16 h) and 60 °C (4 h). The ambient temperature inside the glovebox T_1 was maintained at 30 °C.

While finite element analysis can be used to calculate the induced biaxial stress magnitude in each specimen, it requires LLZTO's CTE value; the following procedure was used obtain it. A bonded LLZTO/epoxy/Si assembly was mounted on a closed-loop heating stage with the Si side facing upward and the temperature was raised gradually. Due to the CTE mismatch between the three materials, the Si substrate develops curvature. Since the LLZTO specimen dimensions are different from those of the substrate, the substrate curvature is non-uniform in general. A multi-beam optical stress sensor (MOSS [47]) setup was used to measure the curvature of the substrate as a function of temperature at the center of the area where LLZTO was bonded. For a temperature change from 30°C to 80°C, the curvature change was seen to be linear, indicating elastic response of the system. The CTE of LLZTO was then obtained by modeling the experiment through finite element analysis (using the published CTE values of Si and epoxy) and a best fit of the model predictions with the measured curvature change. More details are given in the supplemental material. The procedure was repeated for three specimen assemblies and the average inferred CTE value of LLZTO was experiment was $11.3 \pm 2.4 \times 10^{-6}\ \mathrm{K}^{-1}$.

Using the above value of the CTE of LLZTO, the biaxial stress magnitudes for all 18 samples, spanning six curing conditions, were determined by finite-element simulations and are summarized in Table 1. Specimen to specimen variations in the stress state are due to differences in their dimensions. Although the goal was to obtain equi-biaxial stress states, note that variations in specimen dimensions result in minor differences in the stress magnitude along the principal directions.

Table 1. In-plane biaxial stress states for the samples used in this study ($\sigma_{12} = 0$).

Group	Substrate	Curing Temperature	$(\sigma_{11}, \sigma_{22})$ (MPa) for Sample-a	$(\sigma_{11}, \sigma_{22})$ (MPa) for Sample-b	$(\sigma_{11}, \sigma_{22})$ (MPa) for Sample-c
1	Al	30	(0, 0)	(0, 0)	(0, 0)

2	Al	40	(-10.5, -9.2)	(-9.9, -9.4)	(-9.2, -7.4)
3	Al	60	(-33.9, -25.7)	(-26.6, -28.0)	(-27.5, -23.6)
4	Al	80	(-48.0,-58.3)	(-43.5,-47.9)	(-46.9, -51.1)
5	Si	45	(3.6, 3.3)	(4.7, 4.4)	(4.2, 4.8)
6	Si	60	(10.5, 9.9)	(13.5, 15.0)	(9.8, 8.9)

Electrochemical Testing and Optical Imaging

Electrochemical measurements were performed using a Solartron Analytical CellTest system. Electrical contact to the lithium pads was established with two tungsten microprobes (Figure 7(b)). Probe indentation into soft lithium was minimal and did not affect the effective negative electrode area or the location of dendrite nucleation sites. A unidirectional stepwise current loading protocol was applied. After a 30 s open-circuit period, the current was increased following a logarithmic progression, $\log_{10}\left(\frac{j_{\mathrm{n}}}{j_{\mathrm{ref}}}\right) = -1.1 + 0.1n, n = 1,2,\ldots 21$, where $j_{\mathrm{ref}} = 0.5\ \mathrm{mA/cm^2}$, and the reference area was taken as the Li (−) electrode area. Each current step was held for ~30 s, and the voltage was recorded at 1 Hz. The logarithmic step protocol was selected to ensure that the cell assembly reaches a short-circuit before significant stripping-induced contact loss occurs at the Li (+) electrode (due to the limited lithium reservoir on the stripping side).

In situ optical imaging of the cell's top surface was performed using a high-resolution camera (5472 × 3648 pixels, ~1 μm/pixel spatial resolution) positioned directly above the plane of the specimen. Illumination was provided by an LED source at a 45° angle relative to the sample surface normal. The oblique angle avoids parallelism with either the in-plane or out-of-plane features, ensuring a sufficient projected area for both orientations to maximize their optical contrast. Optical imaging was initiated simultaneously with the electrochemical measurements and continued until completion of the experiment or the occurrence of a short circuit. Images were acquired at 0.5 Hz throughout the electrochemical sequence, providing sufficient temporal resolution to resolve dendrite nucleation, front evolution, and optical–electrochemical synchronization.

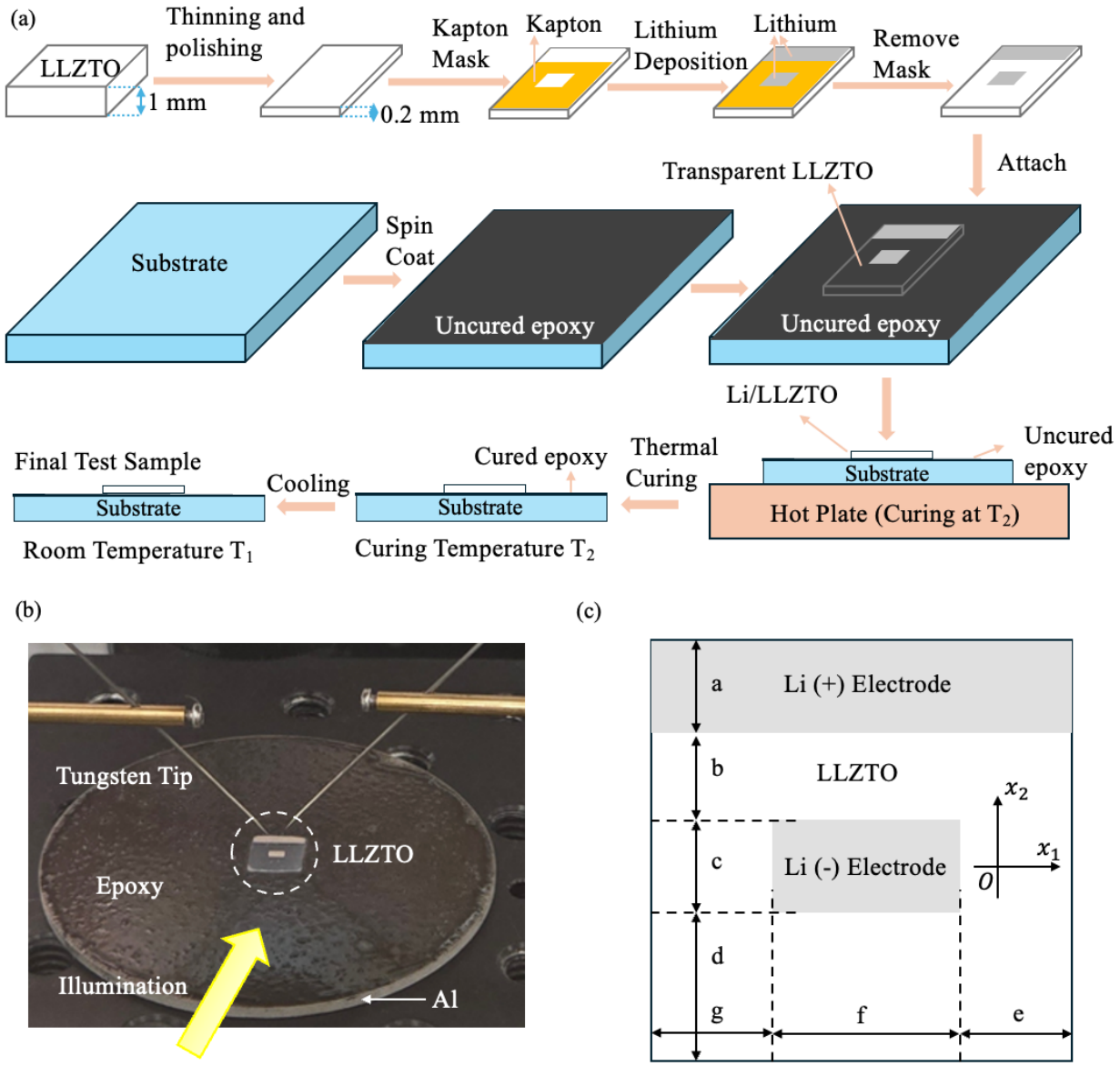


Figure. 7. (a) Sample-preparation procedure; (b) a photograph of the LLZTO/epoxy/Al-substrate assembly mounted on the electrochemical testing stage; (c) schematic top view of the electrode configuration on LLZTO sample surface.

For each acquired image, the RGB data are converted into a grayscale intensity map $I(\mathbf{x};t) \in [0,255]$. To highlight dendrite-induced optical changes, a differential image is further defined as $\Delta I(\mathbf{x};t) = I(\mathbf{x};t) - I(\mathbf{x};0)$. This operation suppresses static intensity variations associated with the initial surface morphology and illumination nonuniformity, thereby enhancing the visibility of dendrite evolution. For improved visualization, the contrast is enhanced using a gamma scaling:

$$\hat{I} = \begin{cases} 128 + 127\left(\frac{\Delta I}{\Delta I_{\max}}\right)^{\gamma}, \text{when } \Delta I \geq 0 \\ 127 - 127\left(\frac{\Delta I}{\Delta I_{\min}}\right)^{\gamma}, \text{when } \Delta I < 0 \end{cases} \quad (1)$$

where $\Delta I_{\max} = \max\left(\Delta I(\mathbf{x}; t_{\text{final}})\right)$, $\Delta I_{\min} = \min\left(\Delta I(\mathbf{x}; t_{\text{final}})\right)$ and $\gamma = \frac{\sqrt{5}-1}{2}$. Using the seismic colormap in Matplotlib, red indicates increased brightness, blue indicates decreased brightness, and white corresponds to regions with negligible change.

SEM/FIB imaging method

Post-experiment characterization of the samples was performed using an FEI Helios 600 DualBeam FIB–SEM and a Thermo Scientific Quattro S scaning electron microscopy (SEM). Before imaging, the vapor-deposited lithium electrode films were removed by gently wiping them with a piece of tissue paper. SEM imaging used a 10 kV accelerating voltage with secondary-electron detection to maximize surface-topography contrast. For subsurface characterization, site-specific FIB cross-sections were prepared at nucleation sites using a Ga^+ beam for trench milling and final polishing. Cross-sectional SEM images were acquired immediately after milling to minimize beam-induced modification.

RESOURCE AVAILABILITY

Lead contact

Further information and requests for resources and materials should be directed to and will be fulfilled by the lead contact, Pradeep R. Guduru (pradeep_guduru@brown.edu).

Materials availability

This study did not generate new unique materials.

Data and code availability

- All data reported in this paper are available from the lead contact upon reasonable request.

- This paper does not report original code.

- Any additional information required to reanalyze the data reported in this paper is available from the lead contact upon reasonable request.

ACKNOWLEDGEMENT

This work has been supported by the Office of Naval Research through grants: N00014-21-1-2815, N00014-23-1-2688, and N00014-26-1-2135. (Program Manager: Dr. Scott Higgins).

AUTHOR CONTRIBUTIONS

S.S. conducted the investigation, developed the methodology, performed formal analysis and data curation, and prepared the original draft. A.P. contributed to the methodology and writing – review & editing. L.C., B.W.S., and K.-S.K. contributed to conceptualization and writing – review & editing. P.R.G. contributed to conceptualization, methodology, funding acquisition, supervision, project administration, and writing – original draft and review & editing.

DECLARE OF INTEREST

The authors declare no competing interests.

Declaration of generative AI and AI-assisted technologies in the manuscript preparation process

During the preparation of this manuscript, the authors used ChatGPT (OpenAI) to improve the language, clarity, and readability of selected sentences. The authors reviewed and edited the content as needed and take full responsibility for the content of the published article.

Reference

1. Wang, C., et al., *Garnet-type solid-state electrolytes: materials, interfaces, and batteries.* Chemical reviews, 2020. **120**(10): p. 4257-4300.
2. Zhang, F., et al., *A review of the effect of external pressure on all-solid-state batteries.* Etransportation, 2023. **15**: p. 100220.
3. Ning, Z., et al., *Dendrite initiation and propagation in lithium metal solid-state batteries.* Nature, 2023. **618**(7964): p. 287-293.
4. Gao, H., et al., *Visualizing the failure of solid electrolyte under GPa-level interface stress induced by lithium eruption.* Nature Communications, 2022. **13**(1): p. 5050.
5. Monismith, S., et al., *Harnessing Electrochemical-Mechanical Couplings to Improve the Reliability of Solid-State Batteries.* Advanced Energy Materials, 2024. **14**(9): p. 2303567.
6. Porz, L., et al., *Mechanism of lithium metal penetration through inorganic solid electrolytes.* Advanced Energy Materials, 2017. **7**(20): p. 1701003.
7. Bistri, D., A. Afshar, and C.V. Di Leo, *Modeling the chemo-mechanical behavior of all-solid-state batteries: a review.* Meccanica, 2021. **56**(6): p. 1523-1554.
8. Cao, D., et al., *Lithium dendrite in all-solid-state batteries: growth mechanisms, suppression strategies, and characterizations.* Matter, 2020. **3**(1): p. 57-94.
9. Zhao, J., et al., *In situ observation of Li deposition-induced cracking in garnet solid electrolytes.* Energy & Environmental Materials, 2022. **5**(2): p. 524-532.
10. Sun, H., et al., *In situ visualization of lithium penetration through solid electrolyte and dead lithium dynamics in solid-state lithium metal batteries.* ACS nano, 2021. **15**(12): p. 19070-19079.
11. Lu, M. and S. Xia, *Operando Characterizations of Lithium Penetration-Induced Fracture in Solid Electrolytes.* Experimental Mechanics, 2024. **64**(7): p. 1161-1174.
12. Athanasiou, C.E., et al., *Operando measurements of dendrite-induced stresses in ceramic electrolytes using photoelasticity.* Matter, 2024. **7**(1): p. 95-106.
13. Fincher, C.D., et al., *Electrochemical corrosion accompanies dendrite growth in solid electrolytes.* Nature, 2026: p. 1-6.
14. Mukherjee, D., et al., *Ingress of Li into solid electrolytes: Cracking and sparsely filled cracks.* Small Structures, 2023. **4**(9): p. 2300022.
15. Fincher, C.D., et al., *Controlling dendrite propagation in solid-state batteries with engineered stress.* Joule, 2022. **6**(12): p. 2794-2809.
16. Kinzer, B., et al., *Operando analysis of the molten Li| LLZO interface: understanding how the physical properties of Li affect the critical current density.* Matter, 2021. **4**(6): p. 1947-1961.
17. Cui, T., et al., *Dendrite initiation and deflection in biaxially stressed solid electrolytes.* Nature, 2026: p. 1-7.
18. Yu, Z., et al., *Dendrite suppression in garnet electrolytes via thermally induced compressive stress.* Joule, 2026. **10**(1).
19. Barroso-Luque, L., Q. Tu, and G. Ceder, *An analysis of solid-state electrodeposition-induced metal plastic flow and predictions of stress states in solid ionic conductor defects.* Journal of The Electrochemical Society, 2020. **167**(2): p. 020534.
20. Feng, M., J. Pan, and Y. Qi, *Impact of electronic properties of grain boundaries on the solid electrolyte interphases (SEIs) in Li-ion batteries.* The Journal of Physical Chemistry C, 2021. **125**(29): p. 15821-15829.

21. Zhang, B., et al., *Atomic mechanism of lithium dendrite penetration in solid electrolytes.* Nature Communications, 2025. **16**(1): p. 1906.
22. Liu, H., et al., *Dendrite formation in solid-state batteries arising from lithium plating and electrolyte reduction.* Nature Materials, 2025: p. 1-8.
23. Kazyak, E., et al., *Li penetration in ceramic solid electrolytes: operando microscopy analysis of morphology, propagation, and reversibility.* Matter, 2020. **2**(4): p. 1025-1048.
24. Huang, J., et al., *Suppressing Dendrite-Induced Cracking in Solid-State Electrolytes: Pressure Constraints and Mechanical Properties.* ACS Applied Materials & Interfaces, 2025. **17**(41): p. 57142-57160.
25. Doux, J.M., et al., *Stack pressure considerations for room-temperature all-solid-state lithium metal batteries.* Advanced Energy Materials, 2020. **10**(1): p. 1903253.
26. Feng, M., C.-T. Yang, and Y. Qi, *The critical stack pressure to alter void generation at Li/solid-electrolyte interfaces during stripping.* Journal of the Electrochemical Society, 2022. **169**(9): p. 090526.
27. Jia, L., et al., *Li–solid electrolyte interfaces/interphases in all-solid-state Li batteries.* Electrochemical Energy Reviews, 2024. **7**(1): p. 12.
28. Morris, S., et al., *Critical Length Scales to Inhibit Dendritic Fracture in Ion-Exchanged LLZTO.* Advanced Energy Materials, 2026: p. e71296.
29. Thomas, C., et al., *Stress engineering for crack and dendrite prevention in solid electrolytes via ion implantation.* Cell Reports Physical Science, 2025. **6**(4).
30. Jagad, H.D., et al., *Tradeoff between the ion exchange-induced residual stress and ion transport in solid electrolytes.* Chemistry of Materials, 2022. **34**(19): p. 8694-8704.
31. Jagad, H.D., et al., *Ion size effects on the thermodynamic, kinetic, and mechanical properties during ion exchange in solid-state electrolytes.* Chemistry of Materials, 2025. **37**(20): p. 8165.
32. Flatscher, F., et al., *Deflecting dendrites by introducing compressive stress in Li7La3Zr2O12 using ion implantation.* Small, 2024. **20**(12): p. 2307515.
33. Yao, X., et al., *Xenon ion implantation induced surface compressive stress for preventing dendrite penetration in solid-state electrolytes.* Small, 2022. **18**(23): p. 2108124.
34. Siniscalchi, M., et al., *Removal and reoccurrence of LLZTO surface contaminants under glovebox conditions.* ACS Applied Materials & Interfaces, 2024. **16**(21): p. 27230.
35. Okumura, A., H. Fukusumi, and M. Kodama, *Magnetron Sputtering Preserves Solid Electrolyte Toughness after Shot Peening and Enhances Critical Current Density in Lithium-Metal Anode All-Solid-State Batteries.* Electrochemistry, 2025. **93**(9): p. 097001-097001.
36. Kodama, M., K. Takashima, and S. Hirai, *Improvement of lithium-metal electrode performance of all-solid-state batteries by shot peening on solid-electrolyte surface.* Journal of Power Sources, 2022. **537**: p. 231556.
37. Monroe, C. and J. Newman, *The effect of interfacial deformation on electrodeposition kinetics.* Journal of The Electrochemical Society, 2004. **151**(6): p. A880-A886.
38. Monroe, C. and J. Newman, *The impact of elastic deformation on deposition kinetics at lithium/polymer interfaces.* Journal of The Electrochemical Society, 2005. **152**(2): p. A396-A404.
39. Gan, C., et al., *Dendrite-growth resistance in solid state electrolytes.* Available at SSRN 7115586.

40. Zhu, C., et al., *Understanding the evolution of lithium dendrites at Li6. 25Al0. 25La3Zr2O12 grain boundaries via operando microscopy techniques.* Nature communications, 2023. **14**(1): p. 1300.
41. Rice, J., *First-order variation in elastic fields due to variation in location of a planar crack front.* 1985.
42. Gao, H. and J.R. Rice, *Somewhat circular tensile cracks.* International Journal of Fracture, 1987. **33**(3): p. 155-174.
43. Moon, M., et al., *The characterization of telephone cord buckling of compressed thin films on substrates.* Journal of the Mechanics and Physics of Solids, 2002. **50**(11): p. 2355-2377.
44. Zhang, X., E. Detournay, and R. Jeffrey, *Propagation of a penny-shaped hydraulic fracture parallel to the free-surface of an elastic half-space.* International journal of fracture, 2002. **115**(2): p. 125-158.
45. Anderson, K., J. Weritz, and J.G. Kaufman, in *ASM Handbook, Volume 02A - Aluminum Science and Technology*. ASM International.
46. Bhushan, B. and X. Li, *Micromechanical and tribological characterization of doped single-crystal silicon and polysilicon films for microelectromechanical systems devices.* Journal of Materials Research, 1997. **12**: p. 54-63.
47. Sethuraman, V.A., et al., *Real-time stress measurements in lithium-ion battery negative-electrodes.* Journal of Power Sources, 2012. **206**: p. 334-342.
48. Hu, S., et al., *Elastic modulus, hardness, and fracture toughness of Li6. 4La3Zr1. 4Ta0. 6O12 solid electrolyte.* Chinese Physics Letters, 2021. **38**(9): p. 098401.
49. Corporation, H. *LOCTITE STYCAST 2651 with CAT 9 – Technical Data Sheet*. 2019 August 2019 [cited 2025 July]; Available from: https://datasheets.tdx.henkel.com/LOCTITE-STYCAST-2651-CAT-9-en_GL.pdf.
50. Okada, Y. and Y. Tokumaru, *Precise determination of lattice parameter and thermal expansion coefficient of silicon between 300 and 1500 K.* Journal of applied physics, 1984. **56**(2): p. 314-320.
51. Wang, Y., et al., *Thermal properties and lattice anharmonicity of Li-ion conducting garnet solid electrolyte Li 6.5 La 3 Zr 1.5 Ta 0.5 O 12.* Journal of Materials Chemistry A, 2024. **12**(29): p. 18248-18257.

Document S1

S1.1 Thermomechanical Modeling and Verification of the LLZTO/Epoxy/Substrate Assembly

This supplementary note provides the thermo-mechanical analysis supporting Methods for the LLZTO/epoxy/substrate tri-layer structure. The thermo-mechanical behavior was analyzed using three-dimensional (3D) finite element analysis (FEA). Three sets of thermo-mechanical simulations were performed with the following objectives:

(i) A representative model was first established to demonstrate the existence of a nearly uniform equi-biaxial stress region on the top surface of the LLZTO.
(ii) Additional simulations were performed to reproduce the curvature–temperature responses measured by the multi-beam optical sensor (MOSS).
(iii) All 18 specimens were simulated reconstruct the residual stress states of each one under its corresponding curing conditions.
This section focuses on the idealized model described in (i). Section S1.2 presents the MOSS calibration described in (ii), whereas the sample-specific simulations in (iii) are readily constructed using the same modeling procedure.

Model Construction and Material Parameters

A three-dimensional thermoelastic model was constructed in the general-purpose finite element software Abaqus using symmetry so that only one-quarter of the full assembly was modeled. The LLZTO, epoxy, and substrate layers were modeled as perfectly bonded linear-elastic solids. Temperature-dependent material properties for LLZTO, epoxy, Al, and Si were taken from the literature and are summarized in Table S1. Reduced-integration C3D8R elements were used for all layers. Each layer was discretized with five elements through its thickness, while the in-plane mesh size in the LLZTO layer was set to 0.1 mm. Logarithmically graded meshes were adopted in the epoxy and substrate layers to accurately resolve the steep interfacial shear stress gradients. A static thermoelastic analysis was performed. Rigid-body motion was eliminated by constraining a single reference node, and a uniform 1 K temperature increment was applied to the entire assembly through a predefined temperature field. Owing to the linear thermoelastic response of the system, the resulting stress field can be linearly scaled to any prescribed temperature difference. Curvature, in-plane stress fields, and through-thickness stress gradients were extracted from the displacement solution. Mesh convergence was verified by confirming that both the curvature–temperature relationship and the in-plane stress distributions remained unchanged with further mesh refinement.

Table S1 Material Parameters in the Finite Element Simulations

Material	E (GPa)	ν	CTE ($\times 10^{-6}$ K^{-1})
LLZTO	158.5 [48]	0.26 [48]	11.3 (Best Fit. See Note S1.2)
Epoxy [49]	4.4	0.39	43.3
Aluminum 6061 [45]	68.9	0.33	23.6

Silicon (<100>)	179 [46]	0.27 [46]	2.5 [50]

Verification of Central Uniform Stress Region

Figure S1 shows the LLZTO/epoxy/silicon assembly, where the dimensions are taken from a representative specimen used for MOSS measurement. When the substrate CTE is lower than that of LLZTO, an increase in temperature induces compressive stress in the LLZTO and causes the specimen assembly to develop a slight curvature. Across the LLZTO thickness (i.e., z-direction) along the symmetry centerline, stress component σ_{11} varies from –0.63 MPa/K at the epoxy interface to –0.35 MPa/K at the top free surface. The in-plane stress components at the top surface of LLZTO (Figure S1(b)) show that a nearly uniform biaxial stress state results within a 1-mm radius from the sample center. Outside this central region, shear-lag effects lead to stress nonuniformity. Hence, the Li (−) electrodes are deposited within the central region of uniform and approximately equi-biaxial stress state in all experiments. The epoxy layer experiences a biaxial stress magnitude of approximately 0.26 MPa/K; so, even for a 100 K thermal excursion, the resulting stress remains below its reported yield strength [49], confirming its elastic behavior during curing and cooling.

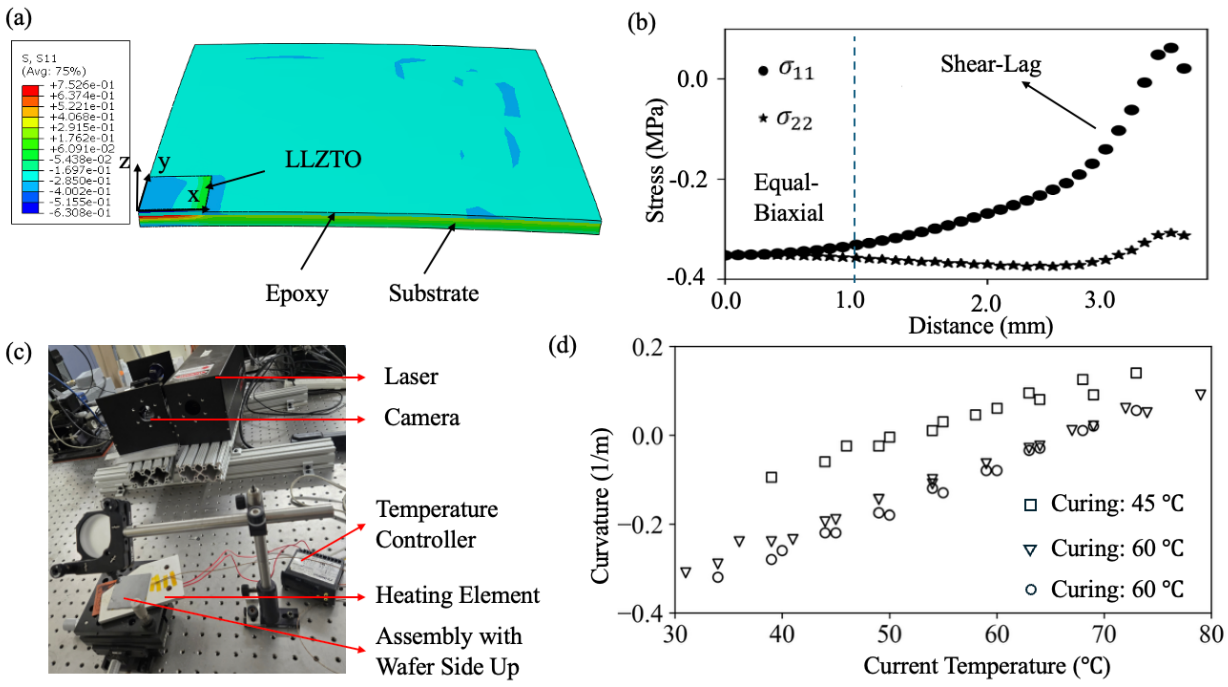


Figure S1. (a) Contour plot of the minimum principal stress from FEM simulation under a 1K temperature increase; (b) the corresponding stress distribution along the horizontal symmetry line (i.e. *x*-axis) where the dashed line indicates the approximate boundary of a central region of uniform and equi-biaxial stress. (c) A photograph of the multi-beam optical sensor setup. (d) Temperature-dependent curvature measured on the Si-side of the LLZTO/epoxy/Si specimen assembly. Curvature was extracted from a 2.2 mm × 2.2 mm central square region (±1.1 mm from the geometric center) by averaging MOSS line scans along the *x*- and *y*-directions. Data for three separate specimens are shown, two of which were cured at 60 °C and one at 45 °C.

S1.2 Experimental Measurement of the Coefficient of Thermal Expansion of LLZTO

This Supplementary Note supports the Methods section by experimentally validating the linear thermo-mechanical response of the LLZTO/epoxy/Si assembly and determining the coefficient of thermal expansion (CTE) of LLZTO. The procedure consisted of measuring the specimen curvature as a function of an imposed temperature increase. A finite element analysis (FEA) of the specimen's response under a temperature change was carried out. The analysis used published thermal and mechanical properties of the constituent materials while treating the CTE of LLZTO as the fitting parameter. The latter was obtained by best-fitting the computationally predicted curvature with the experimental measurement. Details are provided below.

Specimens preparation

Three additional LLZTO/epoxy/Si specimens, separate from the 18 specimens used for electrochemical testing listed in Table 1, were prepared following the procedure described in Methods. Two assemblies were cured at T_2 = 60 °C, and one was cured at T_2 = 45 °C, where T_1 and T_2 denote the measurement and curing temperatures, respectively, as defined in Figure 7(a). The curing temperatures were intentionally selected to fall within the actively controlled measurement temperature range (T_1 = 30–80 °C), allowing the temperature difference $T_2 - T_1$ to take both positive and negative values. For the LLZTO/epoxy/Si assembly, the material combination and geometry remain fixed, so the thermally induced stress and resulting curvature are governed by the temperature difference relative to the curing state. This enables characterization of the thermomechanical response under both positive and negative curvature conditions. No lithium electrodes were incorporated into these specimens, as they were prepared exclusively for thermomechanical calibration rather than electrochemical testing.

Substrate curvature measurement via MOSS

The curvature change of the LLZTO/epoxy/Si specimens was measured using a commercial multi-beam optical sensor (k-Space Multi-beam Optical Sensor) system, which is shown in Figure S1(c). The system projects a 2 × 2 array of parallel laser beams onto the silicon surface of the tri-layer and the reflected array is captured on a CCD camera. As the curvature changes in response to the imposed temperature change, the relative change in the beam spot spacing on the CCD camera is

measured, which is directly proportional to the specimen curvature change. The proportionality constant is obtained by measuring the relative spot spacing corresponding to a calibration mirror of known curvature placed in the plane of the specimen [47]. In a typical experiment, a fully cured LLZTO/epoxy/Si assembly was placed on a closed-loop temperature-controlled stage. The LLZTO side was positioned in contact with the heating plate, while the Si side faced upward to reflect the laser beams in the MOSS setup. The specimen temperature was varied from 30 °C to 80°C in 5 °C increments. At each temperature, the specimen was allowed to reach thermo-mechanical equilibrium until no further relaxation was observed in the MOSS signal. The corresponding curvature was recorded at each temperature. Figure S1(d) shows the data for three experiments, which is used for comparing the FEA analysis predictions.

Finite element analysis

Following the finite element modeling procedure described in Section S1.1, thermo-mechanical simulations were performed for all specimens. At each temperature step, the FEM-predicted average curvature was compared with the experimentally measured curvature. The coefficient of thermal expansion (CTE) of LLZTO was treated as the only unknown material parameter and determined by best-fitting the simulated curvature–temperature response to the experimental measurements. As shown in Figure S1(d), the curvature varies linearly with temperature for all specimens throughout the imposed temperature range. The linear relationship confirms that the LLZTO, epoxy, and silicon layers remain within the linear thermoelastic regime. By fitting the finite element predictions to the experimental curvature–temperature responses, the coefficient of thermal expansion (CTE) of LLZTO was determined to be $11.3 \pm 2.4 \times 10^{-6}\ \mathrm{K}^{-1}$. This value is lower than the XRD-derived value of $17.1 \pm 0.1 \times 10^{-6}\ \mathrm{K}^{-1}$ at 50 °C [51]. The discrepancy is expected because XRD measures the thermal expansion of the crystalline lattice, whereas the present curvature-based method characterizes the effective thermoelastic response of the entire polycrystalline LLZTO bulk. The effective bulk response is influenced by microstructural features such as porosity, dopant distribution, grain-boundary content, and processing history. Therefore, the observed difference is likely attributable to differences in the microstructure. The fitted average CTE was subsequently adopted in all finite element calculations of the residual stress presented in this work.

S1.3 Dendrite Morphology for All 18 Experiments

Final dendrite morphologies for all 18 experiments are provided in Figure S2.

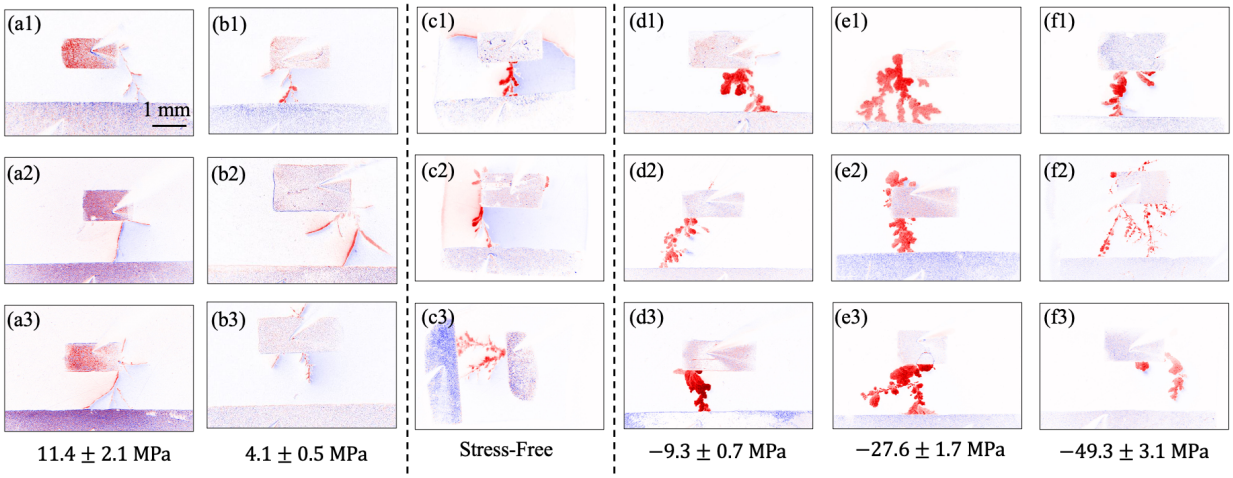


Figure S2. Stress-dependent dendrite morphologies observed in 18 independent LLZTO samples after electrochemical testing. The corresponding stress values are shown for each group of specimens. (a1–a3) 11.4 ± 2.1 MPa; (b1-b3) 4.1 ± 0.5 MPa; (c1–c3) Stress-Free; (d1–d3) −9.3 ± 0.7 MPa; (e1–e3) −28.3 ± 1.7 MPa; (f1–f3) −49.3 ± 3.1 MPa. A single scale bar in (a1) applies to all subpanels. Detailed stress states are given in Table.1. Note that even under compressive stress, occasionally plane-normal dendrites can still nucleate and propagate when the internal lithium pressure overcomes the external compressive stress, but they tend to be less developed as shown in (d1).